A compact matrix model for atrial electrograms for tissue conductivity estimation

Bahareh Abdi[a,*], Richard C. Hendriks[a], Alle-Jan van der Veen[a], Natasja M.S. de Groot[b]

[a] *Circuits and Systems (CAS) Group, Delft University of Technology, the Netherlands*
[b] *Department of Cardiology, Erasmus University Medical Center, the Netherlands*

A B S T R A C T

Finding the hidden parameters of the cardiac electrophysiological model would help to gain more insight on the mechanisms underlying atrial fibrillation, and subsequently, facilitate the diagnosis and treatment of the disease in later stages. In this work, we aim to estimate tissue conductivity from recorded electrograms as an indication of tissue (mal)functioning. To do so, we first develop a simple but effective forward model to replace the computationally intensive reaction-diffusion equations governing the electrical propagation in tissue. Using the simplified model, we present a compact matrix model for electrograms based on conductivity. Subsequently, we exploit the simplicity of the compact model to solve the ill-posed inverse problem of estimating tissue conductivity. The algorithm is demonstrated on simulated data as well as on clinically recorded data. The results show that the model allows to efficiently estimate the conductivity map. In addition, based on the estimated conductivity, realistic electrograms can be regenerated demonstrating the validity of the model.

1. Introduction

Atrial fibrillation (AF) is a common age-related cardiac arrhythmia characterized by rapid and irregular electrical activity of the atria. In Europe, 1–3% of the population (more specifically elderly) suffer from AF. These patients have five times higher risk of strokes, especially ischemic stroke with higher death rate or worse prognosis at higher cost [1]. The development and progression of AF is rooted in impaired electrical conduction and structural damage of atrial tissue, known as electropathology. Electrograms recorded during surgery or high-resolution mappings of the entire atria can help to localize and quantify the degree of electropathology and to stage AF [2,3]. However, the analysis of the electrograms is currently constrained by the lack of suitable methods that can reveal the hidden electrophysiological parameters of the tissue. These parameters can be used as local indication of electropathology in the tissue. The lack of such methods also limits the success rate of some AF therapies, e.g., electrogram-based ablation that targets areas with complex fractionated electrograms. This happens due to the inhomogeneity and complexity in defining fractionation and its relation to pathological causes in tissue [4].

Currently, cardiologists mostly analyze the electrical propagation and electropathology based on local activation times (ATs) and local conduction velocities (CVs), defined as the distance traveled by the depolarization wavefront in a unit of time. However, the interpretation of these propagations, due to the interaction of many parameters, is quite complex, needs expert intervention and is time varying (from beat-to-beat during AF). The changes in conduction velocities may have multiple causes of both pathologic and non-pathologic origin; even pathological causes might not be local and might origin from a different area in the atrium. For example, in a two-dimensional (2D) isotropic and homogeneous tissue, the changes in the propagation velocity from the steady state velocity (for flat wavefront propagation) has a linear relationship with the local curvature [5]. In general, concave wavefronts propagate faster than convex wavefronts without having any pathological causes. CV restitution is another example that influences propagation velocity without indicating electropathology. Using the CV restitution, it has been shown that CV is rate-dependent and typically decreases for shorter inter-beat intervals [6].

The electrical propagation in tissue is governed by electrophysiological models and is directly connected to its underlying parameters. Particularly, the propagation is correlated to the tissue intracellular conductivity. It plays an important role in the underlying dynamics and functional connections in the tissue as a mechanism of inter-cellular communication. The estimation of these hidden parameters can be essential in the diagnosis and staging of the disease. Moreover, the developed physiological models can potentially be used for testing and determining appropriate treatments, e.g., guiding the electrogram based ablation therapies. Unlike CV, analyzing tissue

---

* Corresponding author.
  E-mail address: b.abdikivanani@tudelft.nl (B. Abdi).

conductivity does not require expert intervention and it can be correlated to local electropathology. As an example, it has been shown in previous studies [7,8] that one way to represent fibrosis (as the hallmark of electropathology and AF progression) in computer models of AF is via slow conductivities. Despite the beneficial effect of conductivity in analyzing electropathology, the complexity of the electrophysiological models makes its estimation challenging and not practical in clinical settings.

Realistic computer electrophysiological models of electrograms during sinus rhythm (SR) and AF have been developed in Refs. [9–11]. The results show that an analysis of the morphology of a single electrogram can provide useful information about the substrate maintaining AF. This detailed model is very useful for analyzing the effect of tissue properties like anisotropy and heterogeneity on the resulting electrograms. However, using this model in the inverse problem of extracting tissue properties from electrograms is nearly impossible due to the large number of parameters that need to be estimated. In another study [12], the tissue conductivity map is directly estimated from per cell action potentials (APs) recorded by high resolution micro-electrode arrays, which is not practical for living human tissue. In Refs. [13,14], a quite different approach was used based on Eikonal equations to approximately model the cells' activation times, based on the apparent conductivity while ignoring all the microscopic details of the process, including per cell potentials and electrograms.

Our hypothesis is that understanding atrial fibrillation and improving AF therapy starts by developing a proper forward model that is accurate enough (from a physiological point of view) and simultaneously simple enough to allow for subsequent parameter estimation. Thus, the main focus of this paper is on developing a simplified forward model that can efficiently explain the observed electrogram morphology based on the tissue conductivity. Using a parsimonious parametrization, this model can then be used in the inverse problem of estimating tissue conductivity as an indicator of electrophysiology.

The remainder of this paper is organized as follows. In Section 2 we present the electrophysiological models that describe the electrical propagation and electrogram generation in cardiac tissue. Next, we introduce a simplified matrix model for the electrogram, formulated in terms of two parameter vectors: the activation times and the tissue conductivity map. In Section 3 we formulate the inverse problem of conductivity estimation and present initial algorithms for solving the problem. In Section 4 we demonstrate the performance of our proposed approach on simulated data and compare its results with two other reference approaches. In Section 5 we apply these algorithms to clinically recorded data, and demonstrate their effectiveness in the analysis of real data. We conclude in Section 6, and discuss possible future directions.

2. Electrogram model

2.1. Action potential propagation model

In this study we use the generalized cable theory or the monodomain approach [9] to model the electrical propagation in atrial tissue. In this approach the tissue is discretized on a two (or three) dimensional grid and the electrical propagation (from cell to cell) is governed by a reaction-diffusion equation. Let $V(\mathbf{x}, t)$ be the transmembrane potential of the cell at location $\mathbf{x}$ and time instance t, then the capacitive current through the cell membrane is given by $C\partial V/\partial t$, with $C = 1\,\mu\mathrm{Fcm}^{-2}$ the total membrane capacitance. The reaction-diffusion equation models the membrane current as a function of three currents,

$$C\frac{\partial V(\mathbf{x}, t)}{\partial t} = I_{\mathrm{tm}}(\mathbf{x}, t) + I_{\mathrm{st}}(\mathbf{x}, t) - I_{\mathrm{ion}}(\mathbf{x}, t, V), \tag{1}$$

where I_{st} is the external stimulus current, I_{ion} is the total ionic current based on the Courtemanche model in Ref. [15], and $I_{\mathrm{tm}}(\mathbf{x}, t)$ is the cell

transmembrane current per unit area that accounts for the spatial evolution (diffusion) of the transmembrane potential. It is given by

$$I_{\mathrm{tm}}(\mathbf{x}, t) = S_v^{-1}\nabla\cdot\boldsymbol{\Sigma}(\mathbf{x})\nabla V(\mathbf{x}, t), \tag{2}$$

where $S_v = 0.24\,\mu\mathrm{m}^{-1}$ is the cellular surface to volume ratio, and $\boldsymbol{\Sigma}(\mathbf{x})$ is a location-dependent intracellular conductivity tensor. Eq. (1) can be discretized and solved with no flux boundary conditions, using various approaches including a finite difference method (FDM) for regular rectangular meshes, or using a finite element method (FEM) or finite volume method (FVM) for irregular triangular meshes and curved surfaces.

2.2. Electrogram model

An electrogram is a record of changes in the electrical potential of the (many) cells in the neighborhood of an electrode that is positioned on the heart surface, denoted by $\Phi(\mathbf{y}, t)$, where $\mathbf{y}$ is the location vector of the electrode. The electrogram can be modeled using a current source approximation for a large volume conductor. For a 2D tissue where the modeled cells are located within the area A_0, the electrogram model is [9].

$$\Phi(\mathbf{y}, t) = \frac{1}{4\pi\sigma_e}\int_{A_0}\frac{I_{\mathrm{tm}}(\mathbf{x}, t)}{\|\mathbf{y} - \mathbf{x}\|}\mathrm{d}A(\mathbf{x}), \tag{3}$$

where $A(\mathbf{x})$ is the area variable, σ_e is the constant extra-cellular conductivity, and $I_{\mathrm{tm}}(\mathbf{x}, t)$ is the *trans*-membrane current per unit area as defined in Eq. (2).

To model the measurement process, we develop a space-discretized representation of Eq. (3) for an electrode array. Consider an array of M electrodes, and let $\mathbf{y}_m$ be the location of an electrode with index $m \in \{1,2,...,M\}$. Also let $\mathbf{x}_n$ denote a Δl by Δl discretization of $\mathbf{x}$ with $a = (\Delta l)^2$ the area of each element of the grid and n the index of an element (modeled cell) in the grid. The space-discretized representation of Eq. (3) on a two-dimensional gridded tissue is

$$\Phi_m(t) = \frac{1}{4\pi\sigma_e}\sum_{n=1}^{N}\frac{I_{\mathrm{tm}}(\mathbf{x}_n, t)}{r_{m,n}}a \tag{4}$$

where $\Phi_m(t) \equiv \Phi(\mathbf{y}_m, t)$. In Eq. (4), $r_{m,n}$ denotes the distance between the electrode with index m and the cell with index $n \in \{1,2,...,N\}$ where $N = r_c \times c_c$ is the total number of modeled cells or the elements of the grid with r_c rows and c_c columns. We will assume that the electrodes are also located on a 2D grid parallel to the tissue surface at a height that equals z_0 (we set $z_0 = 1$ mm in the simulations). If we neglect for simplicity the electrode diameter,[1] we can write

$$r_{m,n} = \sqrt{\|\mathbf{y}_m - \mathbf{x}_n\|^2 + z_0^2} \tag{5}$$

and we define $\mathbf{r}_m = [1/r_{m,1}, 1/r_{m,2},...,1/r_{m,N}]^T$ to contain the inverse of the distances of all cells to electrode m.

A space-discretized representation of all per cell transmembrane currents in Eq. (2) is then given by

$$\begin{aligned}I_{\mathrm{tm}}(\mathbf{x}_n, t) &= S_v^{-1}\nabla\cdot\boldsymbol{\Sigma}_n\nabla V_n(t)\\ &= S_v^{-1}(\frac{\partial}{\partial x}(\sigma_{xx,n}\frac{\partial V_n}{\partial x}) + \frac{\partial}{\partial x}(\sigma_{xy,n}\frac{\partial V_n}{\partial y}) + \frac{\partial}{\partial y}(\sigma_{yx,n}\frac{\partial V_n}{\partial x}) + \frac{\partial}{\partial y}(\sigma_{yy,n}\frac{\partial V_n}{\partial y}))\end{aligned} \tag{6}$$

where $\boldsymbol{\Sigma}_n \equiv \boldsymbol{\Sigma}(\mathbf{x}_n)$ and $V(\mathbf{x}_n, t) \equiv V_n(t)$. By stacking all per cell potentials at time instance t in a vector $\mathbf{v}(t) = [V_1(t),...,V_N(t)]^T$ and likewise for the currents $\mathbf{i}_{\mathrm{tm}}(t) = [I_{\mathrm{tm},1}(t),...,I_{\mathrm{tm},N}(t)]^T$, Eq. (6) can be expressed in a space-discretized vector form as

$$\mathbf{i}_{\mathrm{tm}}(t) = S_v^{-1}\mathbf{D}_\sigma\mathbf{v}(t). \tag{7}$$

---

[1] Although generally the electrode diameter needs to be considered, our simulation has a relatively large spatial step size Δl, while the electrode diameter is smaller than Δl.
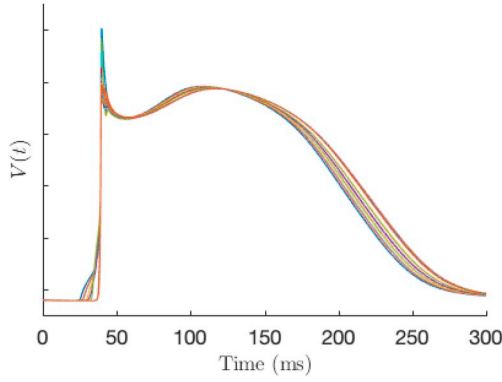
Fig. 1. Aligned simulated APs of the 29th row of the simulated tissue M3 whose conductivity map and activation map are plotted in Fig. 2.

The linear operator $\mathbf{D}_\sigma$ in this equation equals

$$\mathbf{D}_\sigma = \mathbf{D}_x \text{diag}(\sigma_{xx})\mathbf{D}_x + \mathbf{D}_x \text{diag}(\sigma_{xy})\mathbf{D}_y + \mathbf{D}_y \text{diag}(\sigma_{yx})\mathbf{D}_x + \mathbf{D}_y \text{diag}(\sigma_{yy})\mathbf{D}_y,$$
(8)

where $\text{diag}(\cdot)$ is a diagonal matrix with its diagonal entries from the argument vector, and σ_{xx}, σ_{xy}, σ_{yx} and σ_{yy} are vectors stacking the corresponding conductivities of all cells. As an example, $\sigma_{xx} = [\sigma_{xx,1}, \sigma_{xx,2}, ..., \sigma_{xx,N}]^T$. Matrices $\mathbf{D}_x$ and $\mathbf{D}_y$ are respectively the first-order discrete spatial derivative operators in the x and y directions, where we can use a forward, backward, or central space difference scheme.

By using Eq. (7), we can reformulate Eq. (4) as

$$\Phi_m(t) = k \, \mathbf{r}_m^T \mathbf{D}_\sigma \mathbf{v}(t),$$
(9)

where all constants are collected in $k = a(4\pi\sigma_e S_v)^{-1}$. This equation shows that each electrogram is a weighted sum of all per cell action potentials, where the weights depend linearly on the inverse of cell distances to the electrode and nonlinearly on their conductivities.

To develop the space-discretized matrix representation of Eq. (3),

we stack the M electrogram signals in a single vector $\boldsymbol{\phi}(t) = [\Phi_1(t), ..., \Phi_M(t)]^T$. We also define an $M \times N$ matrix $\mathbf{R}$ that contains all the inverse distances from electrodes to cells, $\mathbf{R} = [\mathbf{r}_1, \mathbf{r}_2, ..., \mathbf{r}_M]^T$. Sampling over time, the linearized matrix representation of the electrogram array at all time instances can then be written as

$$\Phi = k \, \mathbf{R} \, \mathbf{D}_\sigma \, \mathbf{V},$$
(10)

where $\Phi = [\boldsymbol{\phi}(0), \boldsymbol{\phi}(1), ..., \boldsymbol{\phi}(T-1)]$ is an $M \times T$ matrix containing all the M resulting electrograms for all time instances, and matrix $\mathbf{V}$ contains all the per cell action potentials.

2.3. Simplified electrogram model

Given an electrogram array Φ, our aim is to estimate the conductivity tensor Σ from Eq. (10). Therefore, we first need to compute $\mathbf{V}$ using Eq. (1). However, we propose to simplify the electrogram model by skipping the transmembrane potential computation in Eq. (1), and benefit from the observation that once activated, all cells produce almost the same stereotype AP, denoted by $V_0(t)$. A similar approach was first employed by Spach et al. in Ref. [16] to reproduce experimental electrograms using the activation times and a stereotype AP. Moreover, the same concept was used by Franzone et al. [17] to model electrograms and look at tissue properties on more complex electrogram morphologies. Both studies verify this assumption and show that it can provide realistic electrograms. To demonstrate this hypothesis, as an example, Fig. 1 shows all simulated action potentials in the 29th row of the anisotropic tissue M3 in Fig. 2. This row includes an area with slower conductivities. The APs have been aligned with respect to their ATs. As can be seen, the depolarization phase of the simulated APs, that are of importance in calculating electrograms, match reasonably with each other. We will discuss the simulations in more details in Section 4.

With this assumption, our proposed simplified matrix representation of Eq. (10) can be written as

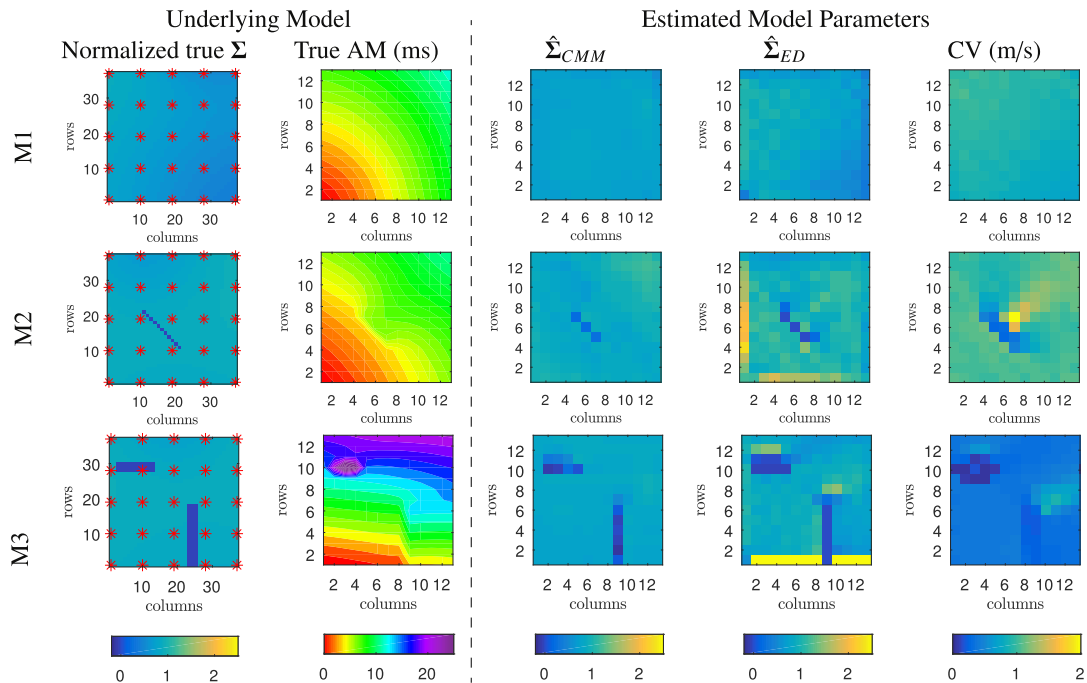$$\Phi = k \, \mathbf{R} \, \mathbf{D}_\sigma \, \mathbf{V}_\tau,$$
(11)

Fig. 2. Each row of the figure demonstrates a simulated tissue and its estimated parameters. First and second columns demonstrate the underlying model including the true conductivity map and the true AM on the 2D tissue surface, respectively. In all cases the tissue is stimulated from the left bottom corner. The electrode locations are indicated by *. The third to fifth columns demonstrates the estimated parameters including conductivity map estimated from the proposed CMM, conductivity map estimated from the Eikonal diffusion equation, and the conduction velocity map, respectively.

where the (n, j) th entry of $\mathbf{V}_\tau$ equals $[\mathbf{V}_\tau]_{n,j} = V_0(jT_s - \tau_n)$, which is a time shifted and sampled version of $V_0(t)$, τ_n is the activation time of cell n, and T_s is the sampling period. This also assumes each cell is activated only once (i.e., data contains a single beat). We will collect all activation times in a vector $\tau = [\tau_1, ..., \tau_N]^T$. The calculation of these delays and their interrelations (e.g., direction and speed of propagation) are not part of this model. This sparse parametrization of the model in terms of τ and σ opens up new possibilities for parameter estimation (conductivity) and further signal manipulations.

2.4. Compact matrix model for electrograms based on conductivity

To this end, we reformulate Eqs. (8) and (11) in the form of a measurement equation that highlights the linear dependency on the conductivity map. As a first step, the conductivity tensor can be written as

$$\Sigma_n = \begin{bmatrix} \sigma_{xx,n} & \sigma_{xy,n} \\ \sigma_{yx,n} & \sigma_{yy,n} \end{bmatrix} = \sigma_n \mathbf{A}_n \begin{bmatrix} 1 & 0 \\ 0 & \alpha_n^2 \end{bmatrix} \mathbf{A}_n^T. \tag{12}$$

The right-hand side of this equation represents an eigenvalue decomposition of the conductivity tensor. The principal eigenvalue σ_n describes the conductivity in the main direction of the cell while α_n defines the anisotropic ratio (for human atrial cells, α_n is of the order of 0.4 [13]). The columns of the orthonormal matrix $\mathbf{A}_n$ are the eigenvectors of the conductivity tensor and define the orientation of the cell in the global coordinate system. $\mathbf{A}_n$ is parametrized by θ_n, a rotation angle that represents the fiber direction. The conductivity tensor can thus be written as

$$\Sigma_n = \sigma_n \mathbf{K}_n, \quad \mathbf{K}_n = \begin{bmatrix} \kappa_{n,1} & \kappa_{n,2} \\ \kappa_{n,3} & \kappa_{n,4} \end{bmatrix}, \tag{13}$$

where $\mathbf{K}_n$ is parametrized by two parameters, α_n and θ_n.

The remaining parameters are then the per cell conductivities along the main direction, i.e., σ_n. Using a stacked vector notation for all cells $n \in \{1, ..., N\}$ we obtain $\sigma = [\sigma_1, \sigma_2, ..., \sigma_N]^T$. Using Eq. (13), Eq. (8) can be written as

$$\begin{aligned} \mathbf{D}_\sigma &= \mathbf{D}_x \text{diag}(\kappa_1)\text{diag}(\sigma)\mathbf{D}_x + \mathbf{D}_x \text{diag}(\kappa_2)\text{diag}(\sigma)\mathbf{D}_y \\ &+ \mathbf{D}_y \text{diag}(\kappa_3)\text{diag}(\sigma)\mathbf{D}_x + \mathbf{D}_y \text{diag}(\kappa_4)\text{diag}(\sigma)\mathbf{D}_y, \end{aligned} \tag{14}$$

where as an example $\kappa_1 = [\kappa_{1,1}, \kappa_{2,1}, ..., \kappa_{N,1}]^T$. We further use a property of the Khatri-Rao product (column-wise Kronecker product) denoted by $\circ$, to write the vectorized form of Eq. (14) to express its linear dependency on σ. The employed property is $(\mathbf{B}^T \circ \mathbf{A})\mathbf{x} = \text{vec}(\mathbf{A}\,\text{diag}(\mathbf{x})\mathbf{B})$, where $\text{vec}(\cdot)$ stacks the columns of the argument matrix to form a vector. The final vectorized version of Eq. (14) is

$$\text{vec}(\mathbf{D}_\sigma) = \Gamma\sigma, \tag{15}$$

where

$$\begin{aligned} \Gamma &= \mathbf{D}_x^T \circ (\text{diag}(\kappa_1)\mathbf{D}_x) + \mathbf{D}_y^T \circ (\text{diag}(\kappa_2)\mathbf{D}_x) + \mathbf{D}_x^T \circ (\text{diag}(\kappa_3)\mathbf{D}_y) \\ &+ \mathbf{D}_y^T \circ (\text{diag}(\kappa_4)\mathbf{D}_y). \end{aligned} \tag{16}$$

Using Eq. (15), and a property of the Kronecker product, denoted by $\otimes$, which is $(\mathbf{B}^T \otimes \mathbf{A})\text{vec}(\mathbf{X}) = \text{vec}(\mathbf{A}\mathbf{X}\mathbf{B})$, we can also present the vectorized version of Eq. (11) as

$$\begin{aligned} \text{vec}(\Phi) &= k(\mathbf{V}_\tau^T \otimes \mathbf{R})\,\text{vec}(\mathbf{D}_\sigma) \\ &= k(\mathbf{V}_\tau^T \otimes \mathbf{R})\,\Gamma\sigma. \end{aligned} \tag{17}$$

Finally, by writing $\phi = \text{vec}(\Phi)$ and defining the mixing matrix $\mathbf{M}_\tau = (\mathbf{V}_\tau^T \otimes (k\,\mathbf{R}))\,\Gamma$ of size $MT \times N$, the resulting linear measurement equation based on conductivity, from here on referred to as the compact matrix model for atrial electrograms (CMM), is

$$\phi = M_\tau \sigma. \tag{18}$$

3. Conductivity estimation

We have seen how the measured data (Φ or ϕ) can be described in terms of a simple parametrization: τ, σ, and some nuisance parameters, i.e., a 2×2 matrix $\mathbf{K}_n$ that models the cell direction. Given the data, the inverse problem is to estimate these parameters. In particular, we are interested in the conductivity map.

An initial step to reduce the number of unknowns and simplify the inverse problem is to estimate the ATs in τ using a standard approach. In this study we estimated τ by finding the minimum of the first time derivative of each electrogram which coincides with the activation time of the cell that is under the electrode [18]. This provides us with an incomplete activation map (AM) where the values are only known for cells that are under the electrodes. Next, we linearly interpolate the incomplete AM to provide a higher resolution AM for modeled cells. This provides a good estimation of ATs when the wavefront is rather smooth and there is only one single wavefront, that is mostly the case during SR. However, our simulation showed that in case of multiple wavefronts or existing blocks in the tissue, that is the case during AF, the activation time estimation using the minimum of the first time derivative of electrograms is less precise and better estimation methods are required. This is deferred to future work.

Assuming τ is known, the next step is to estimate σ using Eq. (18). The amount of data is $M \times T$ while the number of unknown parameters is a function of the chosen spatial resolution, i.e., the modeled number of cells N. As they are both on a regular grid, we can define the ratio of the number of cells with the number of electrodes as the "oversampling ratio" L. The number of unknowns in this step (σ) is then equal to LM. We would expect the number of data samples to be easily larger than the number of unknowns ($T \gg L$), but unfortunately, most time-domain samples are not very informative. Thus, the mixing matrix $\mathbf{M}_\tau$ is ill-conditioned or ill-posed, in particular for larger L. This issue always arises when we discretize and solve an inverse problem that has (i) the form of a first-kind Fredholm integral equation (Eq. (3)), and (ii) has a Laplacian operator (Eq. (1)) in its forward model.

Estimation of the conductivity map σ is based on the linear measurement model Eq. (18). Since the mixing matrix is ill-conditioned, simply inverting $\mathbf{M}_\tau$ produces an unstable solution. Therefore, regularization is needed, which is equivalent to bringing in some prior information to penalize implausible solutions. Our experiments show that, in general, the conductivity in each small enough anatomical site varies smoothly around an average value μ_σ creating a smooth (low rank) conductivity map Σ of size $r_c \times c_c$, where $\sigma = \text{vec}(\Sigma)$. These smooth variations can partly be due to the changes in the properties of many cells in the real 3D tissue that are only modeled by a few cells on the 2D recording area. Notice that the changes in the conductivities of different anatomical sites can also be modeled by setting different values for μ_σ with respect to our prior knowledge of the recording site. On the other hand, in cases of functional or pathological problems, a local conductivity σ_n could be much smaller than the average μ_σ, resulting in a conductivity block that causes irregular AP wavefront propagation or even results in formation of multiple wavefronts.

These observations encourage regularization conditions that promote a sparse and low-rank solution for Σ. Among many possibilities, we will consider the following regularized cost function for estimation of conductivity:

$$J(\sigma) = \|\phi - \mathbf{M}_\tau\sigma\|_2^2 + \lambda_1 \|\sigma - \mu_\sigma \mathbf{1}\|_1 + \lambda_2 \|\Sigma - \mu_\sigma \mathbf{1}\mathbf{1}^T\|_*, \tag{19}$$

where λ_1 and λ_2 are the regularization parameters, and $\mathbf{1}$ is the all-ones vector. The ℓ_1-norm regularization term, $\|\cdot\|_1$, promotes a sparse solution, whereas the nuclear norm $\|\cdot\|_*$ (the sum of singular values of its argument) promotes a smooth low-rank conductivity map. Notice that for applications in which we are more interested in localizing conductivity blocks in tissue, we can ignore the smooth low-rank regularization and only penalize the optimization problem using the ℓ_1-norm which means setting $\lambda_2 = 0$.

In this paper we solve Eq. (19) using the Split Bregman algorithm [19] which leads to the following augmented Lagrangian optimization problem,

$$\hat{\sigma} = \arg\min_{\sigma, \mathbf{p}, \mathbf{Q}} \|\boldsymbol{\phi} - \mathbf{M}_\tau \sigma\|_2^2 + \lambda_1 \|\mathbf{p}\|_1 + \mu_1 \|\mathbf{p} - (\sigma - \mu_\sigma \mathbf{1}) - \mathbf{b}_1\|_2^2 + \lambda_2 \|\mathbf{Q}\|_*$$
$$+ \mu_2 \|\mathbf{Q} - (\boldsymbol{\Sigma} - \mu_\sigma \mathbf{1}\mathbf{1}^T) - \mathbf{B}_2\|_2^2, \qquad (20)$$

where the $\mathbf{p}$ and $\mathbf{Q}$ are the introduced auxiliary variables, μ_1 and μ_2 are penalization parameters, and $\mathbf{b}_1$ and $\mathbf{B}_2$ are the Lagrange multipliers. The Split Bregman algorithm then solves this problem iteratively by breaking it into smaller problems, which are simpler to implement. In each step of each iteration, one unknown parameter is updated by minimizing Eq. (20) while assuming the other unknowns are constant. For more detail on solving each step we refer to Ref. [20]. Overall the algorithm has a fast convergence rate to a reasonable precision in practice.

4. Simulation results

To demonstrate the performance of the proposed conductivity map estimation algorithm, we have simulated 2D phantom tissue areas of 90×90 cells with $\Delta l_0 = 0.02$ cm cell-to-cell distances on the grid, based on examples of real tissue. Each simulated tissue has a different conductivity map with a smooth background and zero, one or two conductivity blocks in it that are respectively shown in the first column of Fig. 2 and are denoted by M1, M2, and M3. Notice that the plots only demonstrate the 37×37 central cells where a 5×5 electrode array with inner-electrode distance of $9\Delta l_0$ was positioned. The electrode locations are shown by the *. The tissues are stimulated with a stimulation current injected to the cell at the left bottom of the tissue. The tissues in M1 and M2 are isotropic ($\alpha_n = 1$) while the tissue in M3 is anisotropic with $\alpha_n = 0.4$. In all simulations $\mathbf{A}$ equals the identity matrix indicating that the main direction of the cells is along the x-axis. Eq. (1) was used to calculate the propagation of the APs on the tissue with a fixed time step $T_s = 0.01$ ms. The resulting activation maps in the selected areas are also shown in the second column of Fig. 2. Eq. (10) was next used to calculate the electrograms recorded by the electrode array. Since this high temporal resolution complicates the succeeding parameter estimation, the resulting electrograms and the stereotype $V_0(t)$ were downsampled by a factor of 5, which increases the sampling period of the data to $T_s = 0.05$ ms. Note that we made sure the upstroke phase of $V_0(t)$ is preserved after down-sampling.

We then use Eq. (20) to estimate the conductivity maps of each tissue, assuming that the isotropic ratio α_n and fiber rotation angle θ_n are known and constant (the same values that were used in generating the data). To reduce the number of unknowns, the modeled cell size in the inverse problem was considered three times bigger than the initial cell size used in the forward model simulation. The inter-electrode distance was considered three times the modeled cell size ($L = 3$), i.e., nine times the initial cell size. To focus on the performance of the conductivity map estimation algorithm itself, and to avoid the errors in AT estimations, we use the real ATs in this simulation. For each modeled cell, we used the activation time of the central cell of the 3×3 block of initial cells that it covers. Obviously using the ATs estimated from electrograms and interpolating them for higher resolution modeled cells introduces inaccuracies in estimating the conductivity map. We will later demonstrate how these inaccurate ATs affect the conductivity estimation. The equations derived in Section 2.4 were then used to calculate the mixing matrix $\mathbf{M}_\tau$, and finally Eq. (20) was used to estimate the conductivity maps. The resulting conductivity maps $\hat{\Sigma}_{CMM}$ are shown in the third column of Fig. 2. Since the focus of this study is on introducing the model itself and not on optimal tuning of its parameters, we used values that yielded visually good results in all simulations, which are, $\lambda_1 = 1e9$, $\lambda_2 = 1e8$, $\mu_1 = 1e4$, $\mu_2 = 1e4$, $\mu_\sigma = 0.9$, and the number of iteration $N_{itr} = 100$.

For reference, we use the apparent conductivity map estimation using the Eikonal-diffusion (ED) equation [14]. To the best of our knowledge, this is the only similar approach that estimates electrical conductivity map and is also applicable to our data. We also provided the local conduction velocity map [21] as a commonly used approach in the literature for analysis of slow conduction and conduction block in tissue. Notice that unlike CMM and ED, CV does not provide a measurement of conductivity but only measures the local velocity of the wavefront propagation. The estimated CV map and the estimated conductivity map from the ED equation, are also plotted in the right two columns of Fig. 2. As shown in the figure, the CV map only provides an overview of areas with fast and slow conduction which cannot be directly connected to tissue conductivity and thus electropathology in tissue. ED, on the other hand, performs well for isotropic and rather homogeneous tissues, but provides inaccurate results around boundaries of the tissue (case M1 and M2), the main diagonal of the coordinate system, and around the boundaries of the blocks. It also completely fails to provide any reliable results in case of anisotropic tissue, which is the case shown in M3. The results in general show that the proposed method outperforms the two reference methods.

Fig. 3 demonstrates two other examples, denoted by M4 and M5. Different from the simulation in Fig. 2, the conductivities are now estimated using the ATs that are estimated from low resolution electrograms instead of using the true ATs. The ATs are estimated by finding the minimum of the first time derivative of electrograms, and linearly interpolated to obtain a higher resolution activation map for all modeled cells. The tissue in M4 is isotropic while the tissue in M5 is anisotropic. All other parameters used in theses simulations are equal to those used in generation of Fig. 2 and only the conductivity maps are different, which are plotted in the first column of Fig. 3. The ground truth ATs and the estimated ATs from electrograms are also shown in Fig. 3. The proposed CMM and ED were used for estimation of conductivity and the results are shown in the last two columns of Fig. 3 respectively. Notice that we did not include CV in this figure. As can be seen, by comparing the estimated AM with the true AM, the estimated ATs are less accurate in areas with blocks. These inaccurate estimations cause the blocks to appear much smoother, or they are even missed. This can also be affected by the size of the block and its geometry with respect to the wavefront propagation direction. As shown in the simulations, the proposed CMM performs better than the ED because it also depends on the final electrograms and not only on the estimated ATs.

Fig. 4 demonstrates the robustness of the model with respect to inaccurate local activation times. The first row shows the estimated conductivity map and conduction velocity map of the simulated tissue M2 that was already presented in Fig. 2. The second to fourth row present three realizations of parameter estimation when uniformly distributed random errors in range of $[-\varepsilon_m, \varepsilon_m]$ ms are added to the true activation times. Note that the average delay between two neighboring modeled cells in the true activation map is about 0.5 ms. The conduction velocity maps are provided for comparison. As can be seen, the conductivity map is less affected by the errors in activation times than CV map due to: (i) its dependency on the electrograms morphology and not only on the estimated activation times, and (ii) the regularization terms in conductivity estimation using Eq. (19).

5. Experiments on clinical data

In this section we apply the proposed method to clinically recorded data. The epicardial electrograms used in this study were recorded using a 192-unipolar electrode array (8×24) with 2 mm inter-electrode distance and 0.45 mm electrode diameter. The electrode array is subsequently positioned on 9 mapping atrial sites using the anatomical borders, visually by the surgeon. The array records 5 s of sinus rhythm and 10 s of induced atrial fibrillation (IAF) signals at each site. This technique was performed in more than 400 patients of 18 years and older, with coronary and/or structural heart disease, with or without
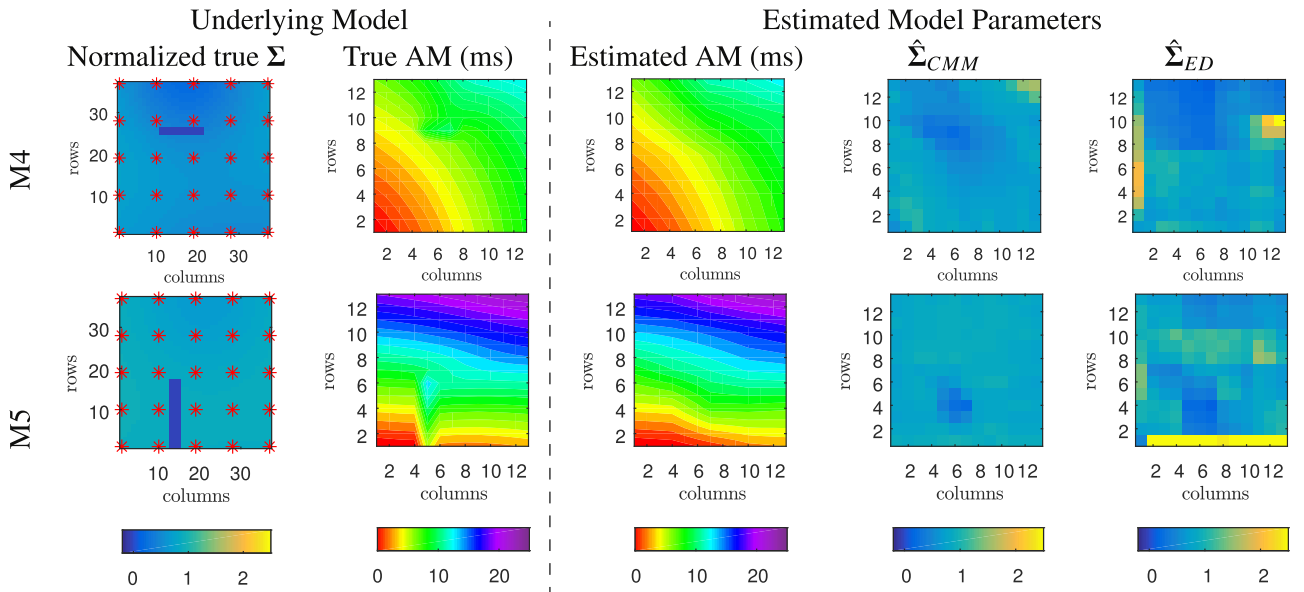
Fig. 3. Each row of the figure demonstrates a simulated tissue and its estimated parameters. First and second columns demonstrate the underlying model including the true conductivity map and the true AM on the 2D tissue surface respectively. In each case the tissue is stimulated from the left bottom corner and the electrode locations are indicated by *. The third to fifth columns demonstrates the estimated parameters including the estimated AM, the estimated conductivity map from the proposed CMM, and the estimated conductivity map from the Eikonal diffusion equation.
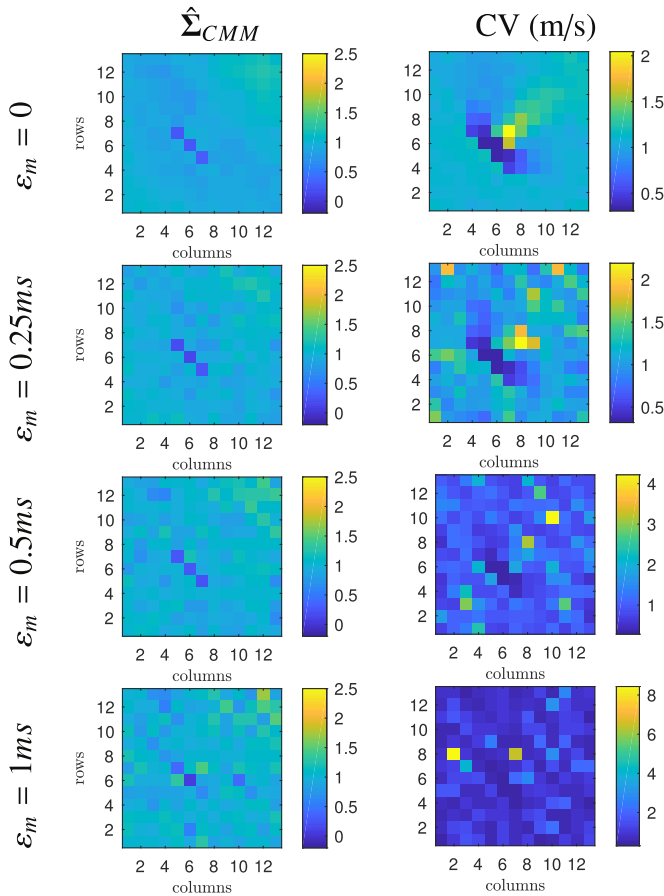
Fig. 4. The first row demonstrates the estimated conductivity map (using the proposed approach) as well as the estimated conduction velocity map for the simulated electrograms already presented in M2 in Fig. 2. The second to fourth row show the same estimated parameters, where uniformly distributed local error, in range of $[-\varepsilon_m, \varepsilon_m]$, are added to the true activation times.

AF, electively scheduled for cardiac surgery and a ventricular ejection fraction above 40%. We have selected four representative patients from the database denoted by P1 to P4, and only used the signals recorded from a fixed location in the middle of the right atrium. The electrograms for P1 to P3 are recorded during SR, and the electrograms for P4 are recorded during IAF. The acquired signals are amplified, filtered (bandwidth 0.5–400 Hz), sampled (1 kHz), analogue to digital converted (16 bits) and recorded on a hard disk. More details on the mapping approach and the electrode array specifications can be found in Ref. [2].

Before employing Eq. (20) to estimate the tissue conductivity, we need to perform some preparation steps. First the tissue surface is meshed with a 2D mono-layer grid where each element on the grid is assumed to be a cell. Although a smaller cell size provides a more accurate estimation of conductivity, to avoid numerical complications and reduce the number of unknowns in our model, we select the largest possible cell size that still reasonably models the electrograms. Therefore, in our simulations the modeled cell size equals $\Delta l = 0.2/3$ cm which is one third of the inner-electrode distance leading to $L = 3$. After gridding the tissue surface the inverse of the cell to electrode distances are calculated and stored in the matrix **R**.

The ATs are estimated using the maximum negative slope of the electrograms followed by a 2D interpolation. This provides good estimates of the ATs under the assumption of SR, and a single smooth wavefront which holds for the P1 to P3. The resulting activation maps are demonstrated in Fig. 5, where the electrode locations are marked by the ∗. We also use the same approach to estimate the ATs for P4 whose activation map is demonstrated in Fig. 6. As can be seen, two wavefronts enter the recording area and collide, and as a result, some electrograms are fractionated. This implies that our approach might provide faulty and smooth ATs that will eventually affect the estimation of conductivity map as already demonstrated in simulated tissues in Fig. 3.

After completing the activation map, we can build $\mathbf{V}_\tau$ in Eq. (11) by shifting the stereotype $V_0(t)$ with respect to the estimated ATs. The matrix $\boldsymbol{\Phi}$ containing the recorded electrograms was initially normalized to have a zero average and a minimum to maximum amplitude of 1. Although we have not measured the tissue fiber direction at the recording site, $\mathbf{A}_n = \mathbf{I}$ for all cells seems reasonable enough with respect to the isochrones geometry. Since the conduction velocity across the x-
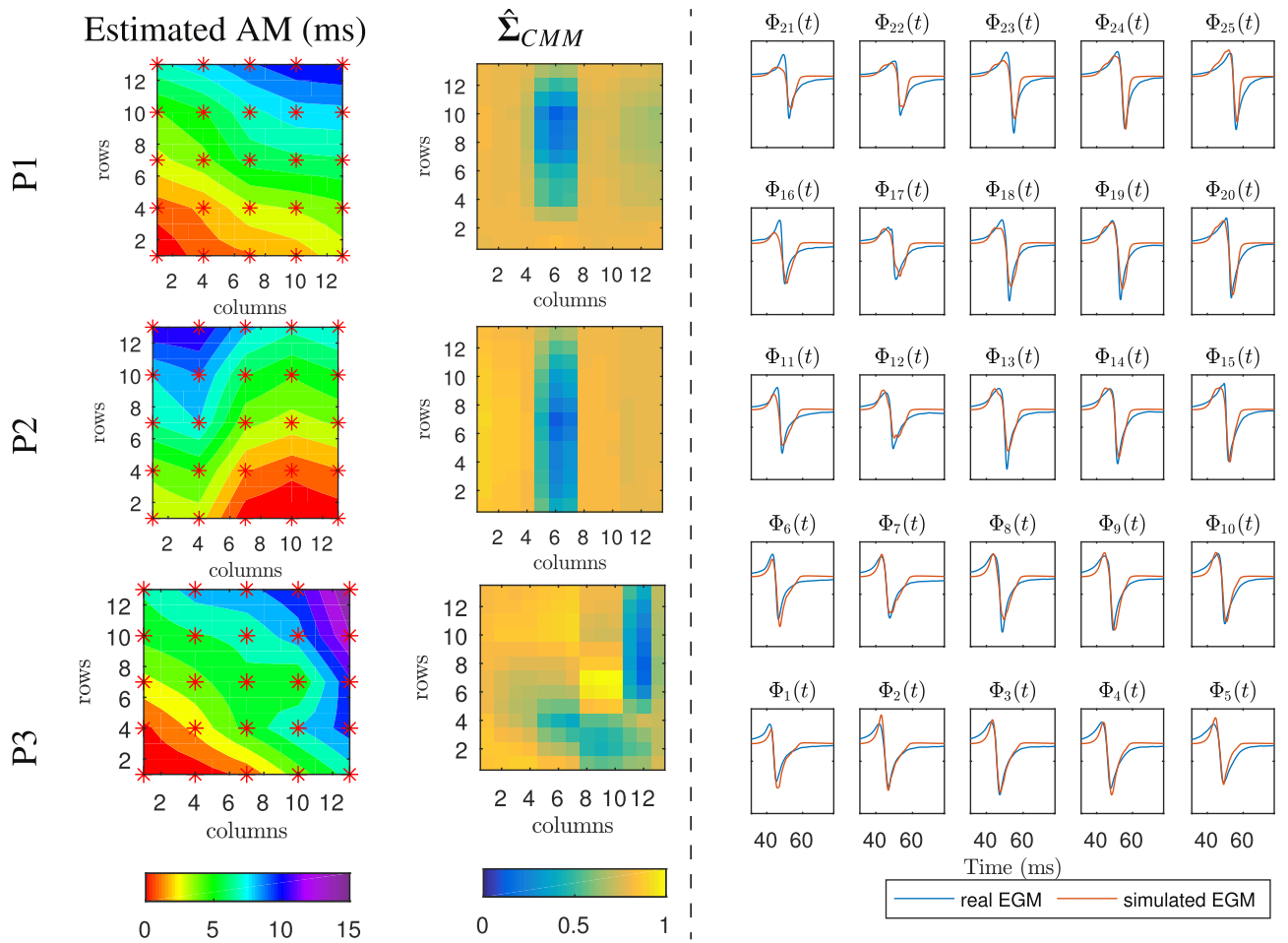
Fig. 5. The estimated activation map (first column) as well as the estimated conductivity map (second column) from the electrograms recorded at the right atrium of three different patients during one heart beat in SR. Clinically recorded electrograms of patients P1, as well as the simulated electrograms using the proposed approach, are also demonstrated in the third column.

axis is almost twice its value across the *y*-axis, we set $\alpha_n^2 = 0.25$. After calculating all necessary parameters, the equations used in Section 2.4 were employed to compute the mixing matrix $\mathbf{M}_\tau$ with $k = 1/300$. Finally, Eq. (20) was used to estimate the conductivity map which are demonstrated in the second column of Figs. 5 and 6. The optimization parameters used in these simulations are $\lambda_1 = 2$, $\lambda_2 = 2$, $\mu_\sigma = 0.8$, $\mu_1 = 1$, $\mu_2 = 1$, $N_{\text{itr}} = 100$. Note that such ranges of variation in the conductivity within a small area is acceptable, as demonstrated in a previous study on similar clinical mapping data [22]. However, these ranges can be further improved by the correct tuning of the regularization parameters. This is deferred to future work.

There is no ground truth to compare the conductivity map to. Therefore, to demonstrate the performance of the model, Fig. 5 also shows the 5×5 clinically recorded electrograms, as well as the modeled electrograms for the same recording in P1. Fig. 6 also demonstrates the recorded and simulated electrograms of P4 during IAF. The estimated σ in combination with the proposed CMM in Eq. (18) were used to generate the modeled electrograms. As we can see, despite the low gridding resolution and all simplifications we made in this study, the real and modeled signals match reasonably, especially around the AT of each electrogram. For IAF data in P4, the approach can, to some extend, follow the morphology of the fractionated electrograms, except for the sharp deflections as in Φ_6. This is partly due to the errors in AT estimation of the fractionated electrograms, and the smooth changes in the AM due to linear interpolations. Moreover, since the electrical propagation outside the boundaries of the simulated tissue is neglected, the simulated electrograms at the boundaries are less accurate.

6. Conclusions and discussion

In this study we developed a compact matrix model for atrial electrograms CMM to show its linear dependence on the conductivity vector, enabling the estimation of this parameter from the recorded electrograms. The results show that despite the low resolution and all simplifying assumptions, the model can efficiently estimate the conductivity map and regenerate realistic electrograms, specially during sinus rhythm. We also provided the results of two other approaches, namely, conductivity estimation based on Eikonal-diffusion equation and conduction velocity estimation. The provided examples show that our method outperforms the other two approaches especially in case of anisotropy and inhomogeneity in the tissue.

However, we need to acknowledge that the presented algorithm may not perform well in cases where our underlying assumptions are not valid. These can happen in two cases. First, when the wavefront is not smooth, as is the case during AF. In this case, multiple wavefronts enter the area of interest simultaneously or one wavefront breaks into multiple wavelets due to the inhomogeneity in the conductivity. This complicates the estimation of the activation times and results in an inaccurate activation map and consequently an inaccurate conductivity map. Therefore, more robust AT estimation algorithms need to be developed. Second, for 3D tissues where each layer of tissue might have a different conductivity map and wavefront propagation. In this case our model, like any other approach that uses electrograms, images all the activities on the 2D tissue surface and ignores the underlying layers and is therefore not valid. Although this can be partly solved by developing
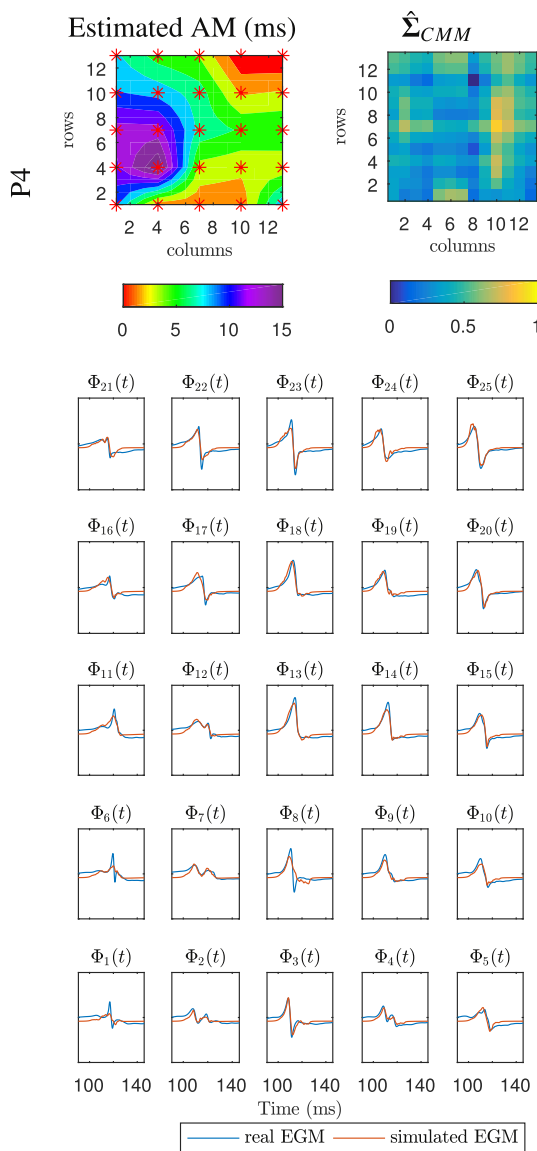
Fig. 6. The estimated activation map (top left) as well as the estimated conductivity map (top right) from the recorded electrograms during induced AF. The recorded electrograms of each electrode as well as the simulated electrograms are also plotted.

3D models of the tissue following the same principles as 2D, the main problem would be the estimation of the ATs in the underlying layers which is currently not possible in clinical recordings.

Future work therefore includes the development of a better algorithm for the estimation of ATs, analyzing the efficiency and accuracy of various alternative regularization functions and algorithms for solving the inverse problem, as well as a discussion on the selection of the regularization parameters.

Conflicts of interest

None declared.

Acknowledgments

References

[1] A.D. Ceornodolea, R. Bal, J.L. Severens, Epidemiology and management of atrial fibrillation and stroke: review of data from four european countries, Stroke Res. Treat. (2017) 1–12 2017.

[2] A. Yaksh, L.J. van der Does, C. Kik, P. Knops, F.B. Oei, P.C. van de Woestijne, J.A. Bekkers, A.J. Bogers, M.A. Allessie, N.M. de Groot, A novel intra-operative, high-resolution atrial mapping approach, J. Intervent. Card Electrophysiol. 44 (3) (2015) 221–225.

[3] E.J. Ciaccio, A.B. Biviano, W. Whang, J.A. Vest, A. Gambhir, A.J. Einstein, H. Garan, Differences in repeating patterns of complex fractionated left atrial electrograms in longstanding persistent as compared with paroxysmal atrial fibrillation, Circulation: Arrhythmia and Electrophysiology 4 (2011) 470–477.

[4] L.J. van der Does, N.M. de Groot, Inhomogeneity and complexity in defining fractionated electrograms, Heart Rhythm 14 (4) (2017) 616–624.

[5] V.G. Fast, A.G. Kléber, Role of wavefront curvature in propagation of cardiac impulse, Cardiovasc. Res. 33 (2) (1997) 258–271.

[6] F.M. Weber, A. Luik, C. Schilling, G. Seemann, M.W. Krueger, C. Lorenz, C. Schmitt, O. Dossel, Conduction velocity restitution of the human atriuman efficient measurement protocol for clinical electrophysiological studies, IEEE (Inst. Electr. Electron. Eng.) Trans. Biomed. Eng. 58 (9) (2011) 2648–2655.

[7] M.W. Krueger, K.S. Rhode, M.D. ONeill, C.A. Rinaldi, J. Gill, R. Razavi, G. Seemann, O. Doessel, Patient-specific modeling of atrial fibrosis increases the accuracy of sinus rhythm simulations and may explain maintenance of atrial fibrillation, J. Electrocardiol. 47 (3) (2014) 324–328.

[8] C.H. Roney, J.D. Bayer, S. Zahid, M. Meo, P.M. Boyle, N.A. Trayanova, M. Haïssaguerre, R. Dubois, H. Cochet, E.J. Vigmond, Modelling methodology of atrial fibrosis affects rotor dynamics and electrograms, EP Europace 18 (suppl_4) (2016) iv146–iv155.

[9] N. Virag, V. Jacquemet, C. Henriquez, S. Zozor, O. Blanc, J.-M. Vesin, E. Pruvot, L. Kappenberger, Study of atrial arrhythmias in a computer model based on magnetic resonance images of human atria, Chaos: Interdiscipl. J. Nonlinear Sci. 12 (3) (2002) 754–763.

[10] V. Jacquemet, N. Virag, Z. Ihara, L. Dang, O. Blanc, S. Zozor, J. Vesin, L. Kappenberger, C. Henriquez, Study of unipolar electrogram morphology in a computer model of atrial fibrillation, J. Cardiovasc. Electrophysiol. 14 (s10) (2003) S172–S179.

[11] V. Jacquemet, A. Van Oosterom, J.-M. Vesin, L. Kappenberger, Analysis of electrocardiograms during atrial fibrillation, IEEE Eng. Med. Biol. Mag. 25 (6) (2006) 79–88.

[12] E. Gilboa, P.S. La Rosa, A. Nehorai, Estimating electrical conductivity tensors of biological tissues using microelectrode arrays, Ann. Biomed. Eng. 40 (10) (2012) 2140–2155.

[13] A.J. Pullan, K.A. Tomlinson, P.J. Hunter, A finite element method for an eikonal equation model of myocardial excitation wavefront propagation, SIAM J. Appl. Math. 63 (1) (2002) 324–350.

[14] P. Chinchapatnam, K.S. Rhode, M. Ginks, C.A. Rinaldi, P. Lambiase, R. Razavi, S. Arridge, M. Sermesant, Model-based imaging of cardiac apparent conductivity and local conduction velocity for diagnosis and planning of therapy, IEEE Trans. Med. Imaging 27 (11) (2008) 1631–1642.

[15] M. Courtemanche, R.J. Ramirez, S. Nattel, Ionic mechanisms underlying human atrial action potential properties: insights from a mathematical model, Am. J. Physiol. Heart Circ. Physiol. 275 (1) (1998) H301–H321.

[16] M.S. Spach, W.T. Miller, P.C. Dolber, J.M. Kootsey, J.R. Sommer, C.E. Mosher, The functional role of structural complexities in the propagation of depolarization in the atrium of the dog. Cardiac conduction disturbances due to discontinuities of effective axial resistivity, Circ. Res. 50 (2) (1982) 175–191.

[17] P.C. Franzone, L. Guerri, M. Pennacchio, B. Taccardi, Anisotropic mechanisms for multiphasic unipolar electrograms: simulation studies and experimental recordings, Ann. Biomed. Eng. 28 (11) (2000) 1326–1342.

[18] C.D. Cantwell, C.H. Roney, F.S. Ng, J.H. Siggers, S. Sherwin, N.S. Peters, Techniques for automated local activation time annotation and conduction velocity estimation in cardiac mapping, Comput. Biol. Med. 65 (2015) 229–242.

[19] T. Goldstein, S. Osher, The split Bregman method for L1-regularized problems, SIAM J. Imag. Sci. 2 (2) (2009) 323–343.

[20] A. Gogna, A. Shukla, H. Agarwal, A. Majumdar, Split Bregman algorithms for sparse/joint-sparse and low-rank signal recovery: application in compressive hyperspectral imaging, Image Processing (ICIP), 2014 IEEE International Conference on, IEEE, 1302–1306, 2014.

[21] G. Salama, A. Kanai, I.R. Efimov, Subthreshold stimulation of Purkinje fibers interrupts ventricular tachycardia in intact hearts. Experimental study with voltage-sensitive dyes and imaging techniques, Circ. Res. 74 (4) (1994) 604–619.

[22] E.A. Lanters, A. Yaksh, C.P. Teuwen, L.J. van der Does, C. Kik, P. Knops, D.M. van Marion, B.J. Brundel, A.J. Bogers, M.A. Allessie, et al., Spatial distribution of conduction disorders during sinus rhythm, Int. J. Cardiol. 249 (2017) 220–225.